ACS Catalysis

Subscriber access provided by Karolinska Institutet, University Library

Article

Self-exfoliated Synthesis of Transition Metal Phosphate Nanolayers for Selective Aerobic Oxidation of Ethyl Lactate to Ethyl Pyruvate

Wei Zhang, Paula Oulego, Sandeep Kumar Sharma, Xiulin
Yang, Lain-Jong Li, Gadi Rothenberg, and N. Raveendran Shiju

ACS Catal., **Just Accepted Manuscript** • DOI: 10.1021/acscatal.9b04452 • Publication Date (Web): 19 Feb 2020

Downloaded from pubs.acs.org on February 27, 2020

Just Accepted

"Just Accepted" manuscripts have been peer-reviewed and accepted for publication. They are posted online prior to technical editing, formatting for publication and author proofing. The American Chemical Society provides "Just Accepted" as a service to the research community to expedite the dissemination of scientific material as soon as possible after acceptance. "Just Accepted" manuscripts appear in full in PDF format accompanied by an HTML abstract. "Just Accepted" manuscripts have been fully peer reviewed, but should not be considered the official version of record. They are citable by the Digital Object Identifier (DOI®). "Just Accepted" is an optional service offered to authors. Therefore, the "Just Accepted" Web site may not include all articles that will be published in the journal. After a manuscript is technically edited and formatted, it will be removed from the "Just Accepted" Web site and published as an ASAP article. Note that technical editing may introduce minor changes to the manuscript text and/or graphics which could affect content, and all legal disclaimers and ethical guidelines that apply to the journal pertain. ACS cannot be held responsible for errors or consequences arising from the use of information contained in these "Just Accepted" manuscripts.

is published by the American Chemical Society. 1155 Sixteenth Street N.W.,
Washington, DC 20036

Published by American Chemical Society. Copyright © American Chemical Society.
However, no copyright claim is made to original U.S. Government works, or works
produced by employees of any Commonwealth realm Crown government in the course
of their duties.

Self-exfoliated Synthesis of Transition Metal Phosphate Nanolayers for Selective Aerobic Oxidation of Ethyl Lactate to Ethyl Pyruvate

Wei Zhang, [1] Paula Oulego, [2] Sandeep K Sharma,[3] Xiu-Lin Yang,[4] Lain-Jong Li,[4] Gadi Rothenberg [1] and N. Raveendran Shiju [1]*

[1] Van 't Hoff Institute for Molecular Sciences, University of Amsterdam, Science Park 904, 1098 XH Amsterdam, The Netherlands.

[2] Department of Chemical and Environmental Engineering, University of Oviedo, C/ Julián Clavería, s/n. E-33071, Oviedo, Spain.

[3] Radiochemistry Division, Bhabha Atomic Research Centre, Mumbai 400 085, India.

[4] Physical Sciences and Engineering Division, King Abdullah University of Science and Technology, Thuwal 23955-6900, Kingdom of Saudi Arabia.

ABSTRACT: Two-dimensional (2D) transition metal nanosheets are promising catalysts because of the enhanced exposure of the active species compared to their 3D counterparts. Here we report a simple, scalable and reproducible strategy to prepare 2D phosphate nanosheets by forming a layered structure *in situ* from phytic acid and transition metal precursors. Controlled combustion of the organic groups of phytic acid results in interlayer carbon which keeps the layers apart during the formation of phosphate and the removal of this carbon results in ultrathin nanosheets with controllable layers. Applying this concept to vanadyl phosphate synthesis, we show that the method yields 2D ultrathin nanosheets of the orthorhombic β-form, exposing abundant V^{4+}/V^{5+} redox sites and oxygen vacancies. We demonstrate the high catalytic activity of this material in the vapor-phase aerobic oxidation of ethyl lactate to ethyl pyruvate. Importantly, these β-$VOPO_4$ do not get hydrated, thereby reducing the competing hydrolysis reaction by water by-product. The result is superior selectivity to ethyl pyruvate compared to analogous vanadyl phosphates. The catalysts are highly stable, maintaining a steady-state conversion of ~ 90% (with >80% selectivity) for at least 80 h on stream. This 'self-exfoliated' synthesis protocol opens opportunities for preparing structural-diverse metal phosphates for catalysis and other applications.

Key words: metal phosphate • β phase • ultrathin nanosheets • heterogeneous catalysis • aerobic oxidation • lactic acid

INTRODUCTION

Ultrathin two-dimensional (2D) materials are attracting increased attention for several applications thanks to their distinctive electronic, optical, semiconducting and catalytic properties.[1-2] Single- or few-layer 2D sheets expose more interior atoms than their bulk counterparts, with abundant surface-active sites and vacancy defects.[3-4] The 2D confinement effect also can shorten mass and heat diffusion pathways. [5] This makes them promising candidates for designing efficient heterogeneous catalysts.[6]

The main state-of-the-art methods for preparing few-layer nanosheets are gas/liquid exfoliation, ion-intercalation or mechanical cleavage.[7] These top-down approaches are suitable for stacked materials with interplanar van der Waals interactions, such as graphene, boron nitride and carbon nitride.[8] Synthesizing 2D nanosheets from non-layered materials is much more difficult.[9] It requires harsh conditions and gives non-uniform thicknesses and low yields.[10] Alternatively, 2D non-layered nanosheets can be produced through template-assisted synthesis,[11-12] surfactant self-assembly,[13-14] oriented attachment growth[15] and inorganic-organic lamellar hybrid intermediates.[16] Yet making high-quality ultrathin nanosheets of non-layered inorganic materials remains a challenge.[17-18]

For example, vanadium phosphates (VPOs) are comprised of alternating vanadium octahedra (VO_6) and phosphate tetrahedra (PO_4).[19] Several crystal structures in different oxidation states are known, such as the V^{5+} vanadyl phosphate (*i.e.,* α_I-, α_{II}-, β-, ω-, δ-, ε- and γ-$V^{V}OPO_4$) and the V^{4+} vanadyl pyrophosphate [$(V^{IV}O)_2P_2O_7$].[20-24] The β phase is thermodynamically the most stable.[25] But since this compact structure has only fewer accessible active sites, its catalytic activity is low.[26] We hypothesized that this problem could be avoided by structuring β-$VOPO_4$ as thin nanosheets, thus exposing more surface V^{4+}/V^{5+} redox couples.[27] $VOPO_4$ nanosheets are currently prepared by an intercalation-exfoliation of bulk α-$VOPO_4{\cdot}2H_2O$ exploiting the weak hydrogen bonds between layers.[28] However, unlike layered α- $VOPO_4$, the 3D network of non-layered β phase is unsuitable for this method, giving no control over the number of layers.

Here we report a new template-free and scalable method for preparing 2D β-$VOPO_4$ ultrathin nanosheets with controlled layers. These sheets are made by self-assembly of vanadyl sulfate ($VOSO_4$) and phytic acid (PTA) precursors, which are abundant and inexpensive; vanadyl sulphate is a byproduct of crude oil refining and phytic acid is a renewable plant-based acid. The phytic acid molecules are the key to this synthesis: (i) they react with $VOSO_4$ as strong chelating agents, suppressing the agglomeration of vanadium species; (ii) they form carbon layers between the vanadium-phosphate complexes from the cyclohexane rings during the

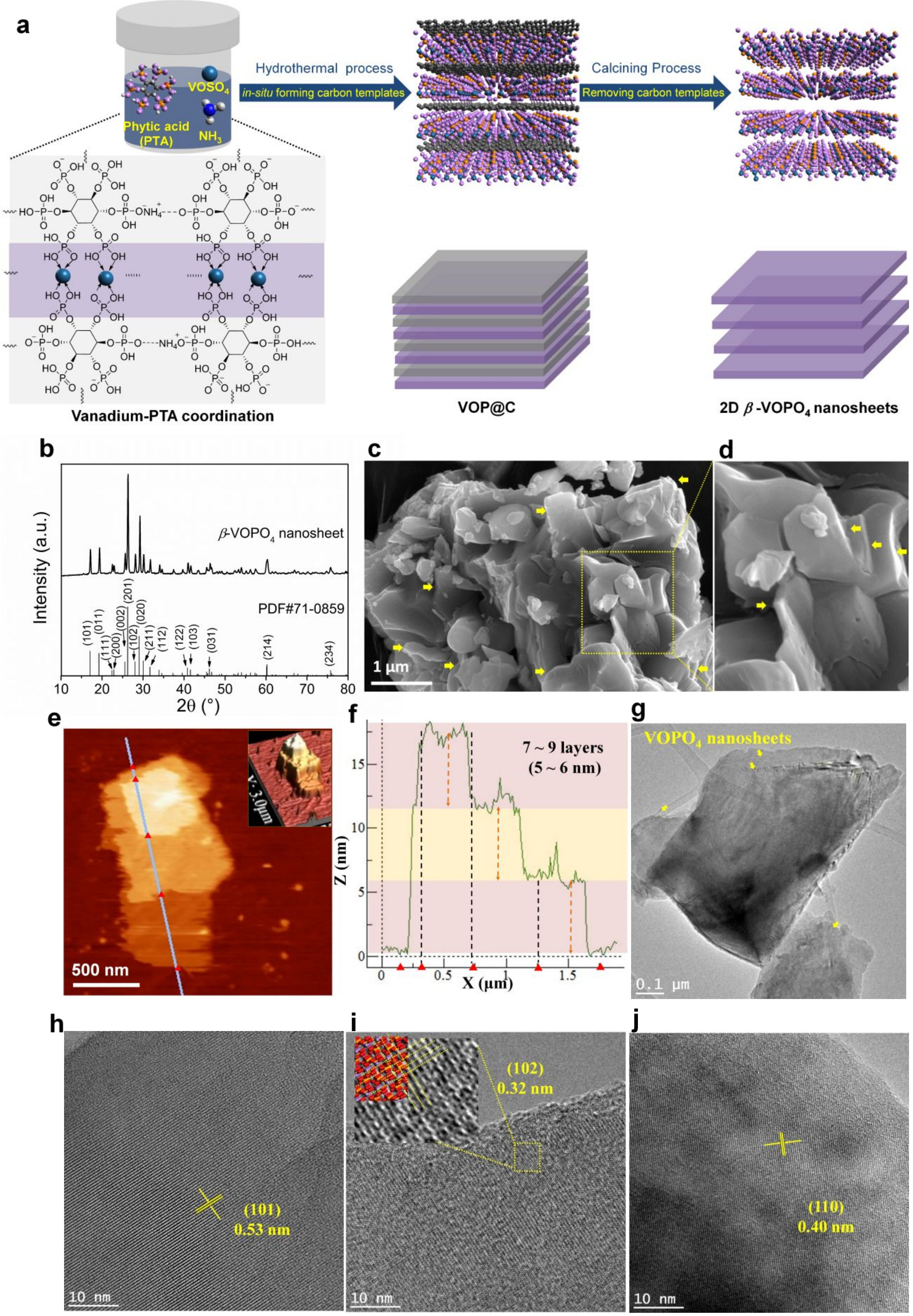

Figure 1. (**a**) Schematic summary of the synthesis procedure for 2D β-VOPO$_4$ nanosheets. (**b**) X-ray diffraction pattern of 2D β-VOPO$_4$ nanosheets (the inset shows the model of layered β-VOPO$_4$); (**c**-**d**) SEM images of β-VOPO$_4$ flakes stacked by layered structure; (**e**) AFM image of few-layer β-VOPO$_4$ nanosheets (inset: the corresponding 3D demonstration); (**f**) The thickness of nanosheets derived from AFM measurement.; (**g**) Representative TEM images of β-VOPO$_4$ nanosheets; (**h**-**j**) Magnified HRTEM images of β-VOPO$_4$ nanosheets taken along [101], [102] and [110] direction.

hydrothermal process. Subsequent pyrolysis removes the PTA,

creating more accessible surface, and increasing the number of V^{4+}/V^{5+} redox sites and oxygen vacancies. This self-exfoliating concept is also general, giving access to various thin transition metal phosphate sheets. We used this method to make active and selective catalysts from inactive forms of phosphates by structuring them as thin nanosheets, thereby exposing more surface active species. The resulting 2D β-$VOPO_4$ ultrathin sheets are excellent catalysts for the vapor-phase air oxidation of ethyl lactate to ethyl pyruvate (Figure S1, see the Supporting Information for full experimental details).

RESULTS AND DISCUSSION

Synthesis and Characterization of β-$VOPO_4$ nanosheets.

Figure 1a illustrates the synthesis strategy for 2D β-$VOPO_4$ ultrathin sheets. In the first step of this simple two-step process, PTA and $VOSO_4$ are dissolved in aqueous solutions, separately. After mixing the two solutions, the vanadium-PTA coordination precursors are formed by the self-assembly of vanadyl ions and PTA. Subsequently, ammonia was added to the mixture adjusting the pH of ~6. Adding ammonia accelerates the complexation, as well as helps to form cross-linked networks by surrounding the vanadium-PTA micelles. The amorphous mixture is then subjected to a hydrothermal treatment (Figure S2). Then, the cyclohexane part of PTA is carbonized, forming VOP@C hybrids. Note that the growth of carbon was restricted between the inter-layers of VOP-PTA hybrids, forming extended 2D carbon layers. In the second step, the *in-situ* formed carbon templates were removed by heat treatment at 550 °C, yielding 2D β-$VOPO_4$ nanosheets.

Powder X-ray diffraction (PXRD) analysis confirmed the formation of pure orthorhombic β-$VOPO_4$ phase (Figure 1b, *cf.* PDF#71-0859). Scanning electron microscopy (SEM) images show the stacked 2D plates with smooth surface, shaped edges and corners, indicating a typical lamellar layered morphology (Figure 1c and 1d). Analysis of the sample by atomic force microscopy (AFM) (Figure 1e and Figure S3) and the corresponding AFM height profile (Figure 1f) indicate that the $VOPO_4$ samples comprise three stacks (see inset in Figure 1e), each with the same average thickness of ~6 nm. This confirms that we successfully synthesized the β-$VOPO_4$ nanosheets with controlled thickness of about 7~8 atomic monolayers. The ultrathin and nearly transparent feature of $VOPO_4$ nanosheets are also shown by transmission electron microscopy (TEM) (Figure 1g), upholding the AFM results. Moreover, the high-resolution TEM (HRTEM) images show the clear lattice fringes with an interplanar distance of 0.53, 0.32 and 0.40 nm (Figure 1h-1j), which can be assigned to the (101), (102) and (110) planes of the β-$VOPO_4$ structure, respectively.

We hypothesized that PTA plays a key role in the formation of 2D β-$VOPO_4$ nanosheets. To test this, we ran a control experiment where, instead of PTA, we used phosphoric acid (H_3PO_4) as P precursor (all other conditions were identical). The resulting $VOPO_4$ material is denoted as PA-VOP O_4. As shown in Figure 2a, the XRD pattern of PA-$VOPO_4$ is almost identical to that of the PTA-derived $VOPO_4$ nanosheets (denoted as PTA-$VOPO_4$), yielding a typical β structure. Unlike layered α-$VOPO_4$ with a 2D anisotropic growth (the adjacent layers are connected with weak van der Waals force),[28] diffraction peaks do not shift in the β phase.[29] However, the ratios of both (011)/ (101) and (002)/(201) planes in PTA-$VOPO_4$ are higher than that of PA-$VOPO_4$ (Figure 2a and Figure S4), probably due to the lamellar layered structure of PTA-$VOPO_4$.

However, an additional peak appeared at 20.3° in PA-$VOPO_4$, which belongs to crystalline V_2O_5. This indicates that some of the vanadyl species are aggregated into V_2O_5. Indeed, a representative HRTEM image of PA-$VOPO_4$ (Figure 2b) confirmed that the V_2O_5 nanocrystallites are dispersed on the $VOPO_4$ matrix. The inset clearly shows lattice fringes of 0.218 nm, corresponding to the (200) lattice space of crystalline V_2O_5. The chemical mapping by energy-dispersive X-ray (EDX) spectroscopy showed the mean atomic V/P ratio of surface PTA-$VOPO_4$ is 0.9 (Table S1), much lower than that of PA-$VOPO_4$ (1.41, see Table S2), indicating the aggregation of vanadia species on the surface of PA-$VOPO_4$.

Both PTA and phosphoric acid are strong chelating agents and coordinate to $VOSO_4$. As shown in Figure 2c, PTA comprises six phosphoric acid attached to a cyclohexane ring. Unlike plain phosphoric acid, the steric hindrance of PTA prevents aggregation during the co-assembly process. Moreover, during the hydrothermal treatment the cyclohexane segments of PTAs are carbonized into a carbon framework, suppressing the agglomeration of vanadium species to V_2O_5. Indeed, after the hydrothermal treatment, the nitrogen sorption isotherm of PTA-derived VOP (PTA-VOP_{HT}) showed increased N_2 uptake in the low relative pressure (P/P_0 <0.1) as well as a hysteresis loop in the region of P/P_0 >0.4, suggesting the formation of a carbon rich in micropores and mesopores (Figure S5a). In contrast, the PA-VOP_{HT} gave negligible N_2 adsorption. Subsequent calcination removes the carbon, giving PTA-$VOPO_4$ showing a steep rise in the range of P/P_0 >0.9 (Figure S5b), which can be assigned to the interlayer voids. We also prepared PA-$VOPO_4$ samples with different $VOSO_4$/PA molar ratios (0.5 and 0.8) under otherwise identical conditions, trying to avoid the formation of crystalline V_2O_5. As is evident from the XRD patterns in Figure S6 in supporting information, crystalline V_2O_5 was present in these samples, further verifying the vital role of phytic acid (PTA) precursor. We conclude that owing to the confined carbonization of PTA, the formed carbon acts as an *in-situ* template, giving the desired few-layer nanosheets. Control experiments wherein the vanadium-PTA complex was directly calcined, without any hydrothermal treatment led to the formation of amorphous VPO (Figure S7), upholding our conclusion.

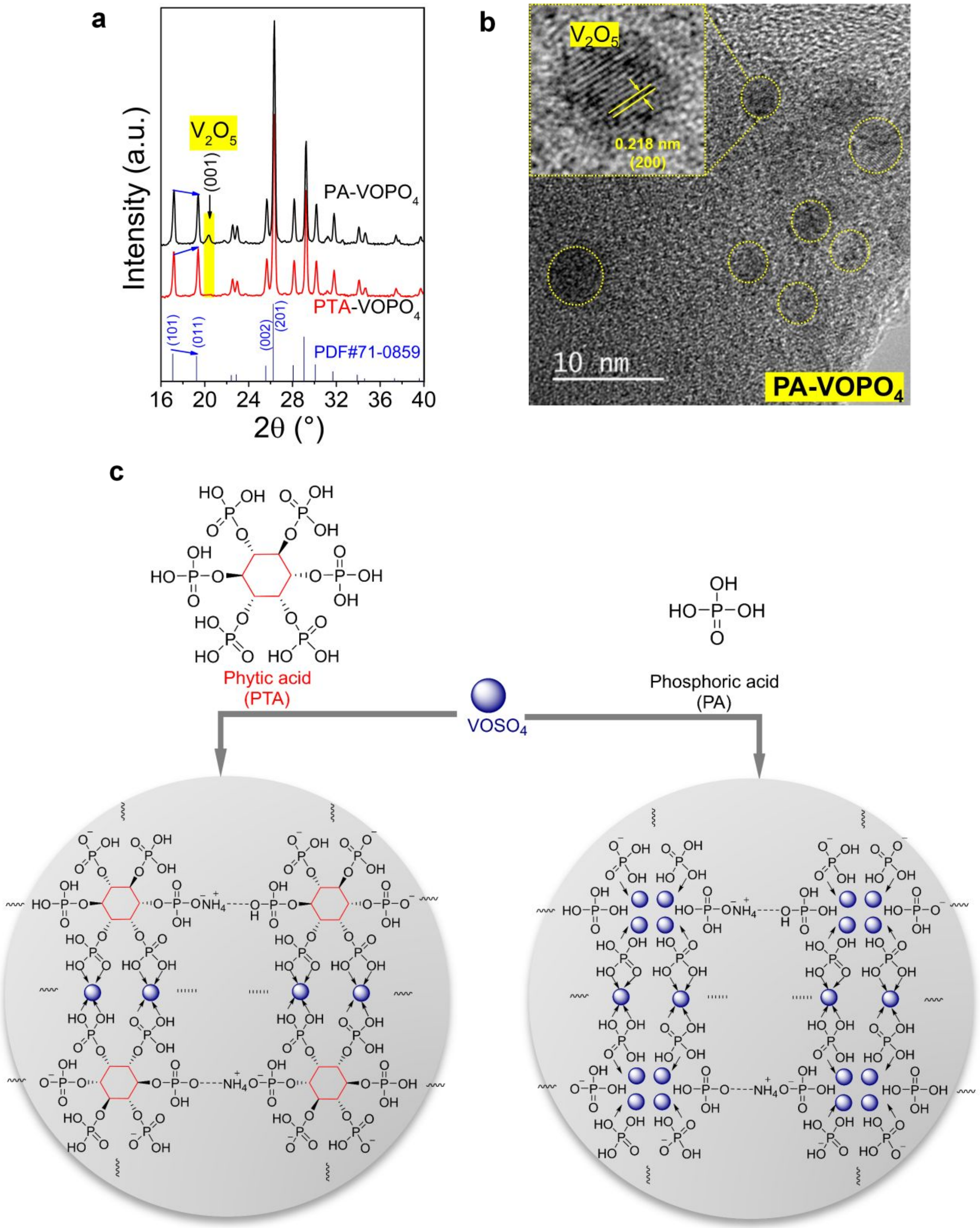

Figure 2. (**a**) Comparison of the X-ray diffraction patterns of two β-$VOPO_4$ catalysts: phytic acid-derived $VOPO_4$ nanosheets (PTA-$VOPO_4$) and the corresponding phosphoric acid-derived $VOPO_4$ (PA-$VOPO_4$); (**b**) Magnified HRTEM images of PA-$VOPO_4$, the inset shows the V_2O_5 nanoparticles with the (200) lattice space. (**c**) Schematic of self-assembly process of $VOSO_4$ and P precursors: phytic acid (PTA) and phosphoric acid (PA).

We then studied the catalytic performance of these β-$VOPO_4$ materials in the vapor-phase oxidative dehydrogenation of ethyl lactate with air to give ethyl pyruvate in a fixed-bed reactor (eq.1). Lactates are biomass-derived “platform molecules” [30] and direct aerobic oxidation of lactate is a sustainable route to bio-based pyruvate, an important intermediate in the food, cosmetics, pharmaceuticals and agrochemicals sectors.[31-32] Previously, we showed that aerobic oxidation of ethyl lactate requires relatively high temperatures. However, the pyruvate is easily over-oxidised on catalyst surface at such high temperatures, lowering the product selectivity. [33] A series of control experiments confirmed that the reaction is in the kinetic regime, with no mass-transfer limitations. Then, we measured the selectivity to ethyl pyruvate against ethyl lactate conversion over phytic acid-derived $VOPO_4$ nanosheets (PTA-$VOPO_4$) and phosphoric acid-derived 3D $VOPO_4$ nanoparticles (PA-$VOPO_4$) (Figure 3a). PTA-$VOPO_4$ outperformed PA-$VOPO_4$ at identical reaction conditions. At the same conversion of ethyl lactate, PTA-$VOPO_4$ is more selective for ethyl pyruvate than PA-$VOPO_4$. The ethyl pyruvate yield at different reaction temperatures were much higher over PTA-$VOPO_4$ nanosheets (Figure 3b), confirming the enhanced catalytic activity. Previously, we demonstrated that this reaction is kinetically favoured in the presence of isolated amorphous vanadium oxide sites, while crystalline V_2O_5 can catalyse this reaction but not selective.[34-35] PA-$VOPO_4$ features well-dispersed V_2O_5 nanocrystals on the surface, yet its catalytic activity and selectively are lower compared to PTA-$VOPO_4$. This is probably because the surface V^{4+}/V^{5+} active sites and oxygen vacancies of PA-$VOPO_4$ are less accessible than those in PTA-$VOPO_4$. We then reasoned that the reactivity enhancement on PTA-$VOPO_4$ is due to the exposed V^{4+}/V^{5+} redox sites and oxygen vacancies.

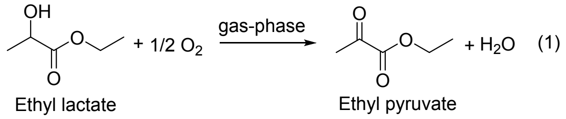

(1)

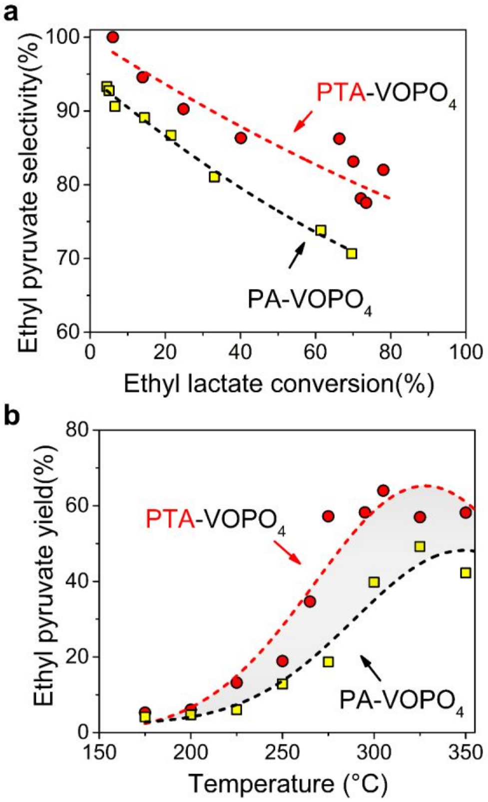

Figure 3. The vapor-phase oxidative dehydrogenation of ethyl lactate with air to give ethyl pyruvate over various β-$VOPO_4$ catalysts: (**a**) Selectivity to ethyl pyruvate plotted against conversion over PTA-$VOPO_4$ and PA-$VOPO_4$. Reaction conditions: Ethyl lactate WHSV=6.25 h^{-1}, air carrier flow rate= 2.25 L/h; (**b**) the corresponding temperature-resolved yield profile of ethyl pyruvate. All data were taken after 2 h on stream.

Factors governing activity and selectivity.

We further characterized the β-$VOPO_4$ sheets to understand this enhanced activity. The full X-ray photoelectron spectroscopy (XPS) survey spectra showed V, P and O in all samples (Figure S8), in accordance with element mapping from high-angle annular dark-field scanning TEM (HAADF-STEM) analysis (Figure 4a and Figure S9). As shown in Figure 4b, the spectra of V 2*p* can be deconvoluted into two peaks centered at 517.2 eV and 518.0 eV, which are associated with V^{4+} and V^{5+} species, respectively. The PTA-$VOPO_4$ nanosheets gave a much higher $V^{4+}/(V^{4+}+V^{5+})$ ratio of 40%, in comparison to 30% in bulk PA-$VOPO_4$ material. Thus, ultrathin nanosheets expose more accessible surface sites, thereby increasing the number of surface V^{4+} species. The enhanced catalytic activity can be assigned to the increased V^{4+}/V^{5+} redox active sites of β-$VOPO_4$ nanosheets.[36] From redox perspectives, introducing V^{4+} into β-$VOPO_4$ nanosheets increases the number of defects and oxygen vacancies. Elsewhere, we have reported that the oxidation of ethyl lactate follows a Mars-van Krevelen mechanism: ethyl lactate adsorbed on the catalytic surface is oxidized by the lattice oxygen, then the resultant oxygen vacancies are replenished by gas-phase oxygen during the oxidation reaction.[33] Thus, both surface lattice oxygens and oxygen vacancies play key roles in aerobic oxidation of ethyl lactate to ethyl pyruvate. These two species can be roughly estimated from the O1*s* XPS spectrum (Figure 4c): the peak at ~532.5 eV can be attributed to the lattice oxygen (O_I), and the peak at ~531.0 eV to the adsorbed oxygen species at the vacancy sites (O_{II}).[4] The O_I peak has a larger area for the PTA-$VOPO_4$ nanosheets than that of PA-$VOPO_4$, indicating that the former exposes more lattice oxygen atoms. Additionally, O_{II} oxygens can enhance the mobility of oxygen species; they are more easily reduced and favorable for the oxidation reaction. PTA-$VOPO_4$ has a higher $O_{II}/(O_I+O_{II})$ ratio, indicating abundant structural defects and oxygen vacancies. Moreover, as the structure defects and oxygen vacancies decrease the electron charge density around phosphorus of PTA-$VOPO_4$, the P $2p_{1/2}$ and P $2p_{3/2}$ peaks shift slightly towards a higher binding energy, in comparison with PA-$VOPO_4$ (Figure 4d).[37]

Further information on the structural defects was obtained from Positron Annihilation Lifetime Spectroscopy (PALS). Figure 4e shows a typical PALS spectrum of PTA-$VOPO_4$. All the PALS spectra could be fitted to two positron lifetime components with a reasonable variance of fit (1.0–1.1). The first positron lifetime ($\boldsymbol{\tau_1}$) in the range of ~208–240 ps is attributed to positron annihilation in the bulk of the materials (see inset in Figure 4e). The longer lifetime ($\boldsymbol{\tau_2}$) in the range of ~ 422-478 ps indicates the presence of larger size defects *i.e.*, vacancy clusters present either in the bulk or at the grain boundaries of the samples. The $\boldsymbol{\tau_1}$ values of PTA-$VOPO_4$ and PA-$VOPO_4$ are nearly the same, showing the identical lattice structure. The intensity corresponding to larger components (I_2) is higher (40%) for nanosheets compared to bulk PA-$VOPO_4$ (36%), suggesting more vacancy defects for PTA-$VOPO_4$ nanosheets. Positrons trapped at the defect sites predominantly annihilate with the surrounding elements and hence provides information about the chemical surrounding. They are efficiently trapped either at negatively charged or neutral open volume defects such as vacancy clusters. According to the crystal structure of the samples, cation vacancy defects (*e.g.* V or P based vacancy defects) are surrounded by oxygen atoms. Figure S10 shows the ratio curves of these samples with respect to a reference Si, in which the peak at P_L ~ $10x10^{-3}$ m_oc indicates the annihilation with the surrounding oxygen atoms at the defect sites. The corresponding peak intensity of PTA-$VOPO_4$ is higher than that of PA-$VOPO_4$, indicating that the defects present in the nanosheets have more O atoms in the surrounding lattice sites. Thus, our ultrathin $VOPO_4$ nanosheets expose more lattice oxygen and oxygen vacancies (Figure 4f), which can explain their high catalytic activity.

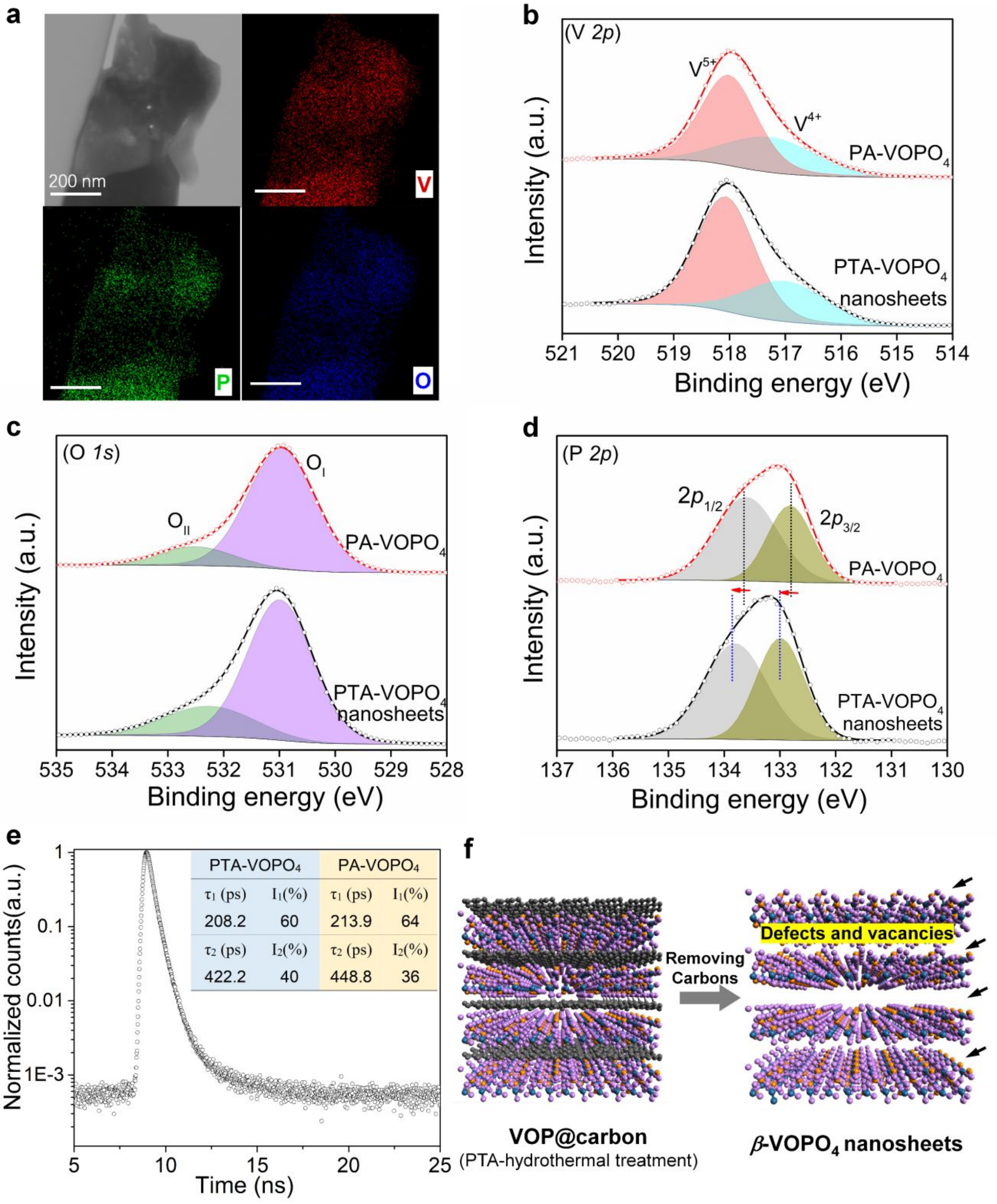

Figure 4. (**a**) STEM image and corresponding elemental mappings of V, P, and O of PTA-$VOPO_4$ nanosheets. XPS studies showing high-resolution V 2*p* spectra (**b**), high-resolution O 1*s* spectra (**c**), and high-resolution P 2*p* spectra (**d**) of PA-$VOPO_4$ and PTA- $VOPO_4$ nanosheets. (**e**) The PALS spectra of PTA-$VOPO_4$ nanosheets (the inset shows the positron annihilation lifetimes and the corresponding intensities in PA-$VOPO_4$ and PTA- $VOPO_4$ nanosheets, respectively). (**f**) Schematic diagram of defects and vacancies, originating from the removal of carbon layers, in PTA-$VOPO_4$ nanosheets.

Self-exfoliated synthesis of other transition metal phosphate nanolayers for catalytic aerobic oxidation of ethyl lactate to ethyl pyruvate.

Based on this 'self-exfoliated' synthesis protocol, we successfully made V, Ni, Co and Fe-based phosphates (see the experimental section in the Supporting Information for details). These desired few-layer nanosheets with the thickness of 2–6 nm were confirmed by HRTEM and AFM analysis (Figure 5, a-c and Figure S11). The combination of XRD, SEM and EDX analysis showed that these phosphates have lamellar layered morphologies with high crystallinity, purity and uniformity (Figure S12-S13 and Table S3-S5, in the supporting information). Thus, our synthesis method is general, facile and scalable via a two-step process (hydrothermal and calcination treatment).

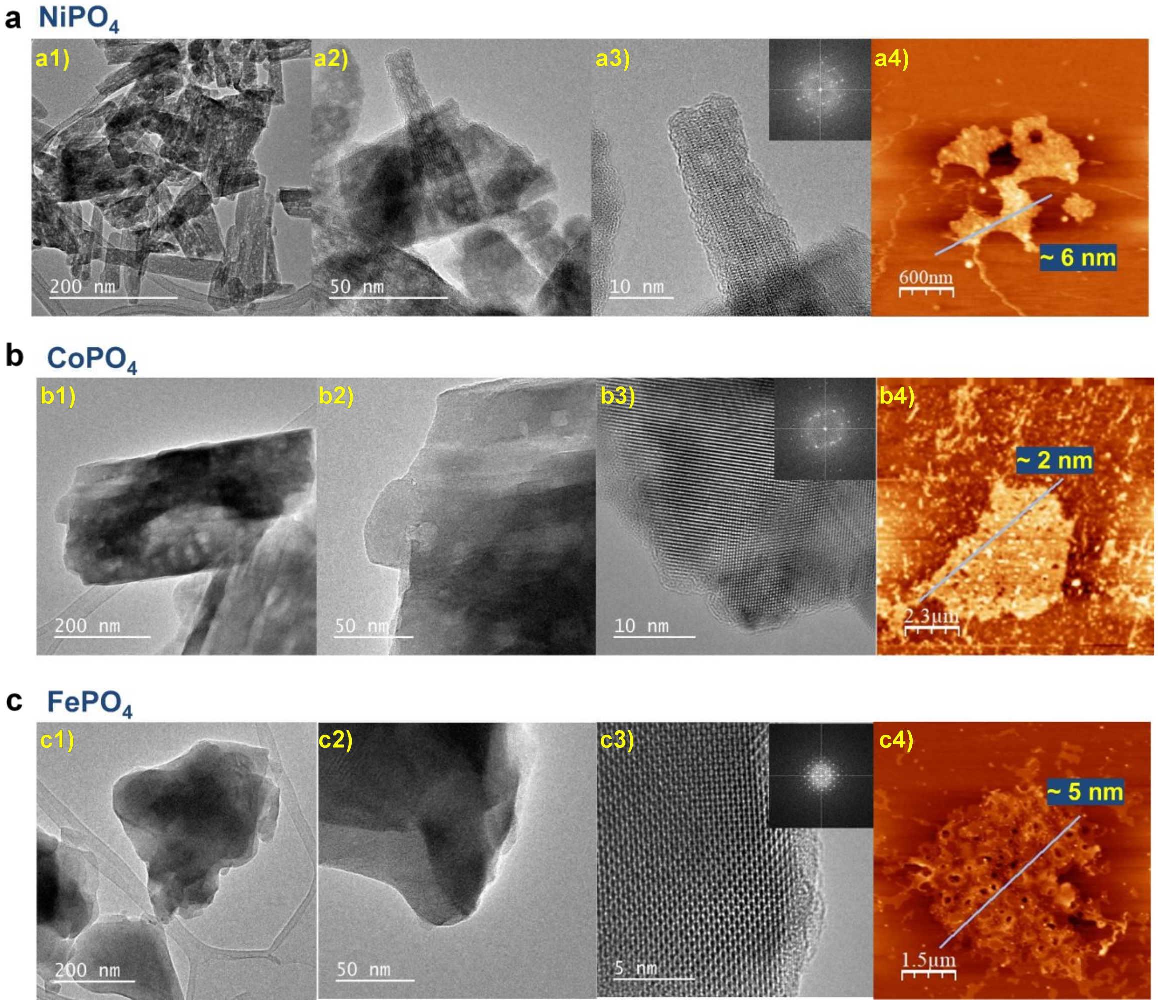

Figure 5. Morphological and microstructural characterization of various phytic acid-derived phosphate nanosheets (**a**-**c**); $NiPO_4$ nanosheets: (a1-a3) TEM images, (a4) AFM image; $CoPO_4$ nanosheets: (b1-b3) TEM images, (b4) AFM image; $FePO_4$ nanosheets: (c1-c3) TEM images, (c4) AFM image. Note: the corresponding height profles of phosphate nanosheets are shown in Figure S11, which derived from AFM measurement.

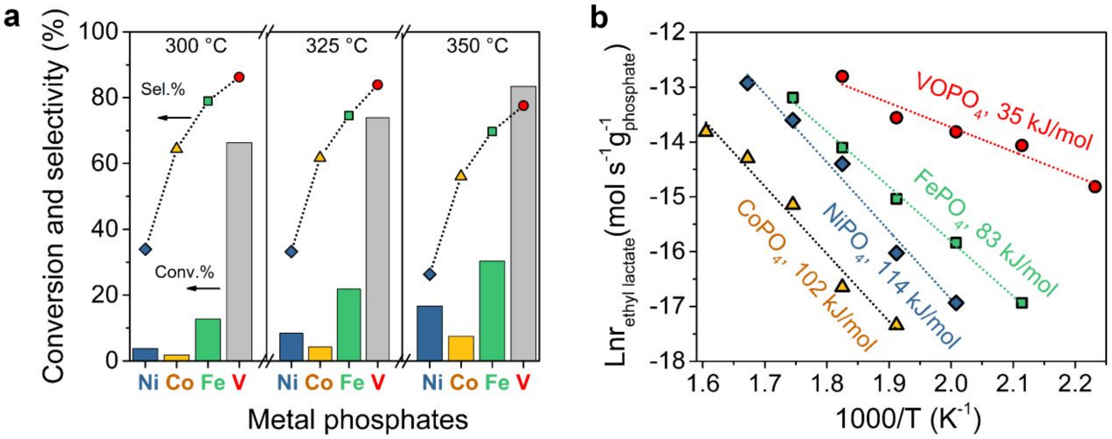

Figure 6. (**a**) Comparisons of ethyl lactate conversion and ethyl pyruvate selectivity over various phytic acid-derived metal phosphate nanosheets: $VOPO_4$, $FePO_4$, $CoPO_4$ and $NiPO_4$. Reaction conditions: Ethyl lactate WHSV=8 h^{-1}, air flow rate= 2.25 L/h, reaction temperature: 300°C, 325 °C and 350 °C. (**b**) Arrhenius plots for steady-state ethyl lactate consumption rate over various phosphate catalysts, the apparent activation energy (E_a) was measured at a series of temperatures below 15 % ethyl lactate conversion.

All the phytic acid-derived phosphate nanosheets were then tested in the vapor-phase aerobic oxidation of ethyl lactate with air at different reaction temperatures (300°C, 325 °C and 350 °C). As shown in Figure 6a, control experiments confirmed that Ni and Co showed some conversion but selectivity to ethyl pyruvate was low, owing to the hydrolysis of ethyl pyruvate on Co- and Ni- phosphate.[36] Intriguingly, $VOPO_4$ nanosheets exhibited the best catalytic performance among all the phosphate catalysts tested in this study, giving a remarkably high activity and selectivity. To better understand this, the apparent activation energies (E_a) were calculated based on Arrhenius plots (Figure 6b), from the data collected below 15% ethyl lactate conversion. The corresponding E_a value for $VOPO_4$ (35 kJ/mol) is much smaller than that for other phosphates: $FePO_4$ (83 kJ/mol), $CoPO_4$ (102 kJ/mol) and $NiPO_4$ (114 kJ/mol). This result confirmed that $VOPO_4$ is intrinsically more active for ethyl lactate oxidation.

Comparisons of catalytic efficiency of various vanadium phosphorus oxides for aerobic oxidation to ethyl lactate.

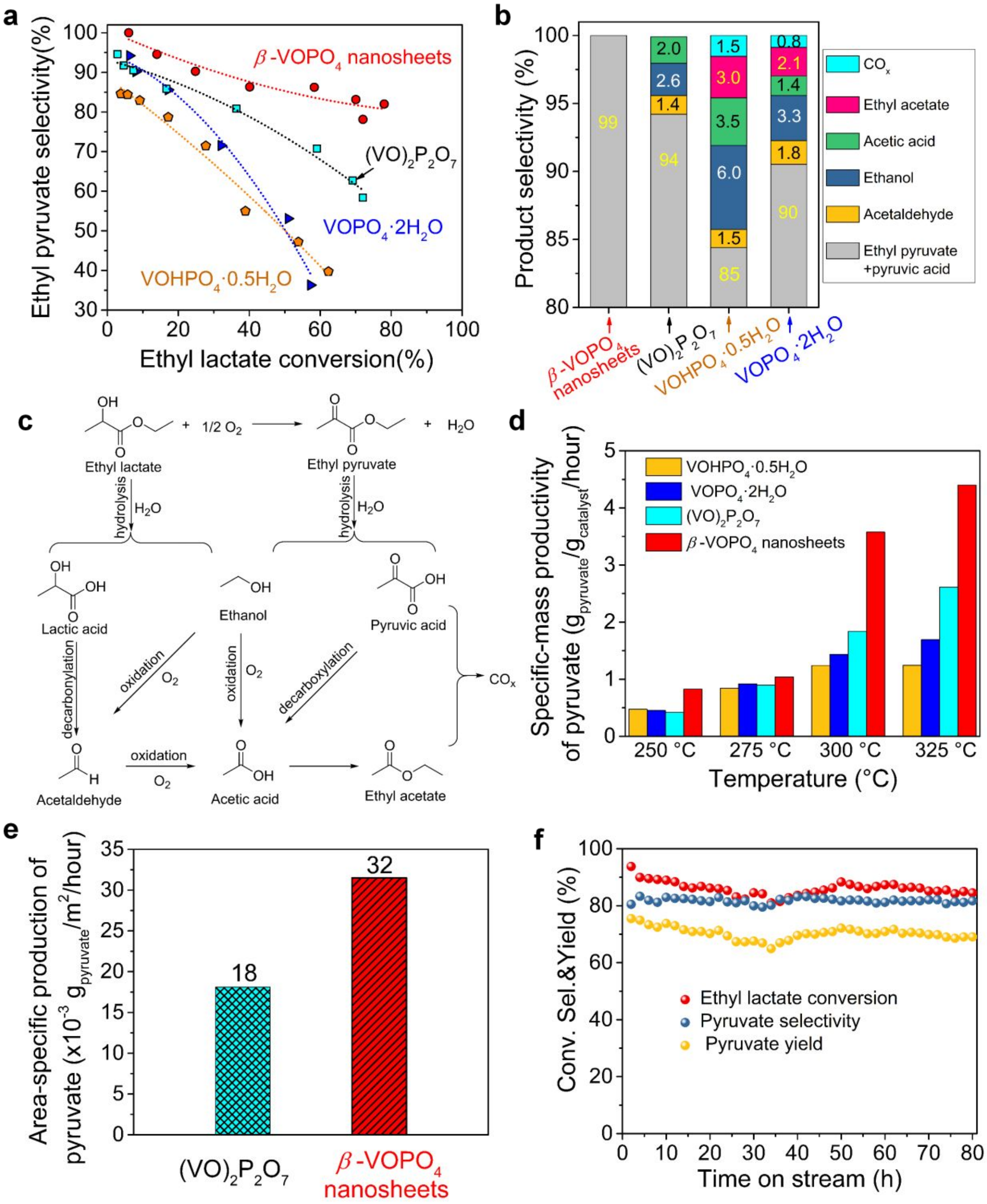

Figure 7. (**a**) Selectivity to ethyl pyruvate plotted against conversion for different VPO catalysts: 2D β-$VOPO_4$ nanosheets, $(VO)_2P_2O_7$, $VOHPO_4{\cdot}0.5\ H_2O$ and $VOPO_4{\cdot}2H_2O$. (**b**) Comparison of the selectivity of various products at ethyl lactate conversion of ~ 6% (β-$VOPO_4$ nanosheets: 6.0 %, $(VO)_2P_2O_7$: 6.2 %, $VOHPO_4{\cdot}0.5\ H_2O$: 5.7 % and $VOPO_4{\cdot}2H_2O$: 6.4 %). The carbon balances were > 98%. (**c**) Reaction pathway for the aerobic oxidation of ethyl lactate on the VPO catalysts. (**d**) The mass-specific activity for pyruvate formation over VPO catalysts in the temperature range 250-325°C. (**e**) Comparisons of the area-specific production rate of pyruvate over 2D β-$VOPO_4$ nanosheets and $(VO)_2P_2O_7$. (**f**) Stability test of the 2D β-$VOPO_4$ nanosheets at optimized conditions (WHSV=3 h^{-1}, T=300 °C).

Olier *et al*. reported that all vanadium phosphorus oxides (VPO) can be hydrated except for β-$VOPO_4$, owing to its highly stable structure.[38] This is consistent with our XPS measurements (Figure 4c), where no surface chemisorbed water was detected (~533 eV). As a result, the competing hydrolysis is suppressed, which may explain why the β-$VOPO_4$ nanosheets gave such high selectivity to pyruvate compared with other metal phosphate catalysts.

To test this, we prepared a series of bulk VPO catalysts for comparison with our nanosheets: vanadyl pyrophosphate [$(VO)_2P_2O_7$], vanadyl phosphate dihydrate ($VOPO_4 \cdot 2H_2O$) and vanadyl hydrogen phosphate hemihydrate ($VOHPO_4 \cdot 0.5H_2O$, see supporting information for full experimental details). Their crystalline structures were confirmed by XRD and Raman spectroscopy (Figure S14 and Figure S15).[39-40] Figure 7a shows the selectivity-conversion plots. All the VPO catalysts were active in lactate-to-pyruvate reaction. Interestingly, β-$VOPO_4$ nanosheets showed highest ethyl pyruvate selectivity, reaching over 90% at ethyl lactate conversion of ~25%. Even at a high ethyl lactate conversion of ~80%, the selectivity is as high as 80% compared with ~60% for $(VO)_2P_2O_7$. Control experiments were performed at a steady-state conversion of ~ 6% for all the tested catalysts (the carbon balances were > 98%) to better differentiate the influence of the VPO phases on product selectivity. As shown in Figure 7b, β-$VOPO_4$ nanosheets gave over 99% *selectivity* to ethyl pyruvate, while a series of by-products were detected on other three VPO catalysts, such as acetaldehyde, ethanol, acetic acid, ethyl acetate and CO_x. This indicates that except for β phase, the VPO catalysts undergoes the competing overoxidation, hydrolysis, decarbonylation and decarboxylation (see Figure 7c). The by-product distribution is different among different catalysts. $VOHPO_4 \cdot 0.5\ H_2O$ and $VOPO_4 \cdot 2H_2O$ gave higher selectivity to ethanol than $(VO)_2P_2O_7$, owing to the hydrolysis of ester on their hydrated surfaces.

We also compared the mass-specific activity (calculated as grams of pyruvate produced per gram of catalyst per hour) over VPO catalysts at different temperatures (Figure 7d). Our β-$VOPO_4$ catalyst outperformed the classical phosphates, especially at high reaction temperatures over 300 °C. Moreover, layered β-$VOPO_4$ and $(VO)_2P_2O_7$ gave similar specific BET areas of 33 m^2/g and 25 m^2/g, respectively, much higher than $VOHPO_4 \cdot 0.5\ H_2O$ (16 m^2/g), $VOPO_4 \cdot 2H_2O$ (9 m^2/g). We then plotted the area-specific catalytic rates for pyruvate production over β-$VOPO_4$ and $(VO)_2P_2O_7$ catalysts. As shown in Figure 7e, the area-specific activity for β-$VOPO_4$ nanosheets is almost twice higher than $(VO)_2P_2O_7$ at 300 °C.The stability and regenerability are key factors for a heterogenous catalyst in its practical application. We tested the stability of our β-$VOPO_4$ nanosheets at optimized conditions (WHSV=3 h^{-1}, T=300 °C, see Table S6). As shown in Figure 7f, this catalyst is highly stable, with a steady-state conversion of ~ 90% (over 80% selectivity) for at least 80 h without significant loss of activity. We also used the same catalyst bed for a series of testing studies, and for this, the catalyst was cleaned and regenerated by simply passing air at 500 °C for 2 h and switching off the ethyl lactate feed. The XRD, TEM and XPS analysis further confirmed that the structure was well preserved after multiple regenerations (Figure S16-S18 in supporting information). Most of 2D nanosheets are still far from commercialisation, because their cost is a problem to scale-up. Our 2D β-$VOPO_4$ nanosheets are promising in this regard, because they can be readily achieved from inexpensive starting materials such as $VOSO_4$ and phytic acid. $VOSO_4$ is a byproduct of crude oil refining (ca. 2000-5000 \$/ton) and PTA is a renewable inexpensive plant-based acid (ca. 6500 \$/ton).[41] The metal salts are also cheap; therefore, these nanosheets are industrially viable catalysts cost wise as well.

CONCLUSIONS

We report the synthesis of 2D ultrathin phosphate nanosheets by a new template-free 'self-exfoliated' strategy using renewable phytic acid (PTA). PTA acts as a strong chelating agent, but can also be carbonized *in situ* into carbon templates, which are responsible for the precisely controlled few-layer nanosheets. Application of this method to vanadium phosphate produces β-$VOPO_4$ ultrathin nanosheets, which expose abundant V^{4+}/V^{5+} redox sites and oxygen vacancies. Importantly, β-$VOPO_4$ does not get hydrated, thereby reducing the competing hydrolysis by water byproduct. These features result in a superior catalytic activity and selectivity in the aerobic oxidation of ethyl lactate to ethyl pyruvate compared to the classical vanadium phosphate. The inexpensive β-$VOPO_4$ nanosheets show good long-term stability and facile recovery. These nanosheets are not only among the best heterogeneous catalysts for the vapor-phase oxidation of lactate to pyruvate, they also show for the first time that the "inert" β-$VOPO_4$ phase can be an efficient oxidation catalyst under the right conditions. Note that this is a general synthesis method, giving access to various metal phosphate nanosheets, such as Ni, Co and Fe. Therefore, this work opens new avenue for the synthesis of new transition metal phosphate nanosheets for catalysis and other applications.

AUTHOR INFORMATION

Corresponding Author

*E-mail: n.r.shiju@uva.nl

ORCID

Wei Zhang: 0000-0003-4506-6583

Gadi Rothenberg: 0000-0003-1286-4474

N. Raveendran Shiju: 0000-0001-7943-5864

Notes

There are no conflicts to declare.

ASSOCIATED CONTENT

Supporting Information

Additional data were listed in the Supporting Information. Experimental procedures, additional characterization data of vanadyl phosphate catalysts including XRD patterns, nitrogen adsorption – desorption isotherms, SEM/TEM/AFM images, EDX spectra, XPS spectra, PALS spectra, Raman spectra and results of reaction parameters on aerobic oxidation of ethyl lactate with air. This information is available free of charge on the ACS Publications website.

ACKNOWLEDGMENT

W. Zhang thanks the China Scholarship Council (201506140058) for a PhD fellowship. P. Oulego thanks the Spanish Ministry of Economy and Competitiveness (MINECO) (Project CTM2015-63864-R) and European Union (FEDER) for funding. This work is part of the Research Priority Area Sustainable Chemistry of the University of Amsterdam, http://suschem.uva.nl.

REFERENCES

(1) Chhowalla, M.; Shin, H. S.; Eda, G.; Li, L.-J.; Loh, K. P.; Zhang, H. The chemistry of two-dimensional layered transition metal dichalcogenide nanosheets. *Nat. Chem.* **2013**, *5*, 263-275.

(2) Ling, T.; Wang, J. J.; Zhang, H.; Song, S. T.; Zhou, Y. Z.; Zhao, J.; Du, X. W. Freestanding Ultrathin Metallic Nanosheets: Materials, Synthesis, and Applications. *Adv. Mater.* **2015**, *27*, 5396-5402.; Gitis, V. ; Chung, S.-H.; Shiju, N. R. *FlatChem* **2018**, *10*, 39.

(3) Hong, J.; Jin, C.; Yuan, J.; Zhang, Z. Atomic Defects in Two-Dimensional Materials: From Single-Atom Spectroscopy to Functionalities in Opto-/Electronics, Nanomagnetism, and Catalysis. *Adv. Mater.* **2017**, *29*. 1606434.

(4) Bi, Y.; Zhang, B.; Wang, L.; Zhang, Y.; Ding, Y. Ultrathin FeOOH Nanolayers with Rich Oxygen Vacancies on BiVO4 Photoanodes for Efficient Water Oxidation. *Angew. Chem. Int. Ed.* **2018**, *57*, 2248-2252.

(5) Xiong, P.; Ma, R.; Sakai, N.; Sasaki, T. Genuine Unilamellar Metal Oxide Nanosheets Confined in a Superlattice-like Structure for Superior Energy Storage. *ACS Nano* **2018**, *12*, 1768-1777.

(6) Ng, W.; Gnanakumar, E.; Rothenberg, G.; Batyrev, E.; Sharma, S.; Pujari, P.; Greer, H.; Zhou, W.; Sakidja, R.; Barsoum, M.; Shiju, N. R. Ti3AlC2 MAX-phase as an efficient catalyst for oxidative dehydrogenation of n-butane. *Angew. Chem. Int. Ed.* **2018**, *57*, 1485-1490.

(7) Yang, W.; Zhang, X.; Xie, Y. Advances and challenges in chemistry of two-dimensional nanosheets. *Nano Today* **2016**, *11*, 793-816.

(8) Geim, A. K.; Grigorieva, I. V. Van der Waals heterostructures. *Nature* **2013**, *499-425*, 419.

(9) Di, J.; Xia, J.; Li, H.; Liu, Z. Freestanding atomically-thin two-dimensional materials beyond graphene meeting photocatalysis: Opportunities and challenges. *Nano Energy* **2017**, *35*, 79-91.

(10) Zhu, W.; Gao, X.; Li, Q.; Li, H.; Chao, Y.; Li, M.; Mahurin, S. M.; Li, H.; Zhu, H.; Dai, S. Controlled Gas Exfoliation of Boron Nitride into Few-Layered Nanosheets. *Angew. Chem. Int. Ed.* **2016**, *55*, 10766-10770.

(11) Huang, X.; Li, S.; Huang, Y.; Wu, S.; Zhou, X.; Li, S.; Gan, C. L.; Boey, F.; Mirkin, C. A.; Zhang, H. Synthesis of hexagonal close-packed gold nanostructures. *Nat. Commun.* **2011**, *2*, 292.

(12) Cheng, W.; He, J.; Yao, T.; Sun, Z.; Jiang, Y.; Liu, Q.; Jiang, S.; Hu, F.; Xie, Z.; He, B.; Yan, W.; Wei, S. Half-Unit-Cell α-Fe$_2$O$_3$ Semiconductor Nanosheets with Intrinsic and Robust Ferromagnetism. *J. Am. Chem. Soc.* **2014**, *136*, 10393-10398.

(13) Wang, J.; Xu, Y.; Ding, B.; Chang, Z.; Zhang, X.; Yamauchi, Y.; Wu, K. C.-W. Confined Self-Assembly in Two-Dimensional Interlayer Space: Monolayered Mesoporous Carbon Nanosheets with In-Plane Orderly Arranged Mesopores and High Graphitized Framework. *Angew. Chem. Int. Ed.* **2018**, *57*, 2894-2898.

(14) Sun, Z.; Liao, T.; Dou, Y.; Hwang, S. M.; Park, M.-S.; Jiang, L.; Kim, J. H.; Dou, S. X. Generalized self-assembly of scalable two-dimensional transition metal oxide nanosheets. *Nat. Commun.* **2014**, *5*, 3813.

(15) Schliehe, C.; Juarez, B. H.; Pelletier, M.; Jander, S.; Greshnykh, D.; Nagel, M.; Meyer, A.; Foerster, S.; Kornowski, A.; Klinke, C.; Weller, H. Ultrathin PbS Sheets by Two-Dimensional Oriented Attachment. *Science* **2010**, *329*, 550-553.

(16) Son, J. S.; Wen, X. D.; Joo, J.; Chae, J.; Baek, S. i.; Park, K.; Kim, J. H.; An, K.; Yu, J. H.; Kwon, S. G.; Choi, S. H.; Wang, Z.; Kim, Y. W.; Kuk, Y.; Hoffmann, R.; Hyeon, T. Large ‐ Scale Soft Colloidal Template Synthesis of 1.4 nm Thick CdSe Nanosheets. *Angew. Chem. Int. Ed.* **2009**, *48*, 6861-6864.

(17) Feng, W.; Zhenxing, W.; Ahmed, S. T.; Yao, W.; Fengmei, W.; Xueying, Z.; Qisheng, W.; Kai, X.; Yun, H.; Lei, Y.; Chao, J.; Jun, H. Two ‐ Dimensional Non ‐ Layered Materials: Synthesis, Properties and Applications. *Adv. Funct. Mater.* **2017**, *27*, 1603254.

(18) Dou, Y.; Zhang, L.; Xu, X.; Sun, Z.; Liao, T.; Dou, S. X. Atomically thin non-layered nanomaterials for energy storage and conversion. *Chem. Soc. Rev.* **2017**, *46*, 7338-7373.

(19) Centi, G.; Trifiro, F.; Ebner, J. R.; Franchetti, V. M. Mechanistic aspects of maleic anhydride synthesis from C4 hydrocarbons over phosphorus vanadium oxide. *Chem. Rev.* **1988**, *88*, 55-80.

(20) Weng, W.; Al Otaibi, R.; Alhumaimess, M.; Conte, M.; Bartley, J. K.; Dummer, N. F.; Hutchings, G. J.; Kiely, C. J. Controlling vanadium phosphate catalyst precursor morphology by adding alkane solvents in the reduction step of VOPO$_4$·2H$_2$O to VOHPO$_4$·0.5H$_2$O. *J. Mater. Chem.* **2011**, *21*, 16136-16146.

(21) Centi, G. Vanadyl Pyrophosphate - A Critical Overview. *Catal. Today* **1993**, *16*, 5-26.

(22) Coulston, G. W.; Bare, S. R.; Kung, H.; Birkeland, K.; Bethke, G. K.; Harlow, R.; Herron, N.; Lee, P. L. The Kinetic Significance of V^{5+} in n-Butane Oxidation Catalyzed by Vanadium Phosphates. *Science* **1997**, *275*, 191-193.

(23) Hutchings, G. J.; Desmartin-Chomel, A.; Olier, R.; Volta, J.-C. Role of the product in the transformation of a catalyst to its active state. *Nature* **1994**, *368*, 41.

(24) Lashier, M. E.; Schrader, G. L. Reactive lattice oxygen sites for C4 hydrocarbon selective oxidation over β-VOPO$_4$. *J. Catal.* **1991**, *128*, 113-125.

(25) Gopal, R.; Calvo, C. Crystal structure of β VPO$_5$. *J. Solid State Chem.* **1972**, *5*, 432-435.

(26) Willinger, M. G.; Su, D. S.; Schlögl, R. Electronic structure of β-VOPO$_4$. *Phys. Rev. B* **2005**, *71*, 155118.

(27) Eichelbaum, M.; Hävecker, M.; Heine, C.; Karpov, A.; Dobner, C.-K.; Rosowski, F.; Trunschke, A.; Schlögl, R. The Intimate Relationship between Bulk Electronic Conductivity and Selectivity in the Catalytic Oxidation of n-Butane. *Angew. Chem. Int. Ed.* **2012**, *51*, 6246-6250.

(28) Wu, C.; Lu, X.; Peng, L.; Xu, K.; Peng, X.; Huang, J.; Yu, G.; Xie, Y. Two-dimensional vanadyl phosphate ultrathin nanosheets for high energy density and flexible pseudocapacitors. *Nat. Commun.* **2013**, *4*, 2431.

(29) Zhang, J.; Zhang, Y.; Zhang, X.; Ling, Y.; Li, F.; Bond, A. Controllable synthesis of few-layer bismuth subcarbonate by electrochemical exfoliation for enhanced CO$_2$ reduction performance. *Angew. Chem. Int. Ed.* **2018**, *57*, 13283-13287.

(30) Beerthuis, R.; Rothenberg, G.; Shiju, N. R. Catalytic routes towards acrylic acid, adipic acid and ε-caprolactam starting from biorenewables. *Green Chem.* **2015**, *17*, 1341-1361.

(31) Xu, P.; Qiu, J.; Gao, C.; Ma, C. Biotechnological routes to pyruvate production. *J. Biosci. Bioeng.* **2008**, *105*, 169-175.

(32) Sugiyama, S.; Kikumoto, T.; Tanaka, H.; Nakagawa, K.; Sotowa, K.-I.; Maehara, K.; Himeno, Y.; Ninomiya, W. Enhancement of Catalytic Activity on Pd/C and Te–Pd/C During the Oxidative Dehydrogenation of Sodium Lactate to Pyruvate in an Aqueous Phase Under Pressurized Oxygen. *Catal. Lett.* **2009**, *131*, 129-134.

(33) Zhang, W.; Innocenti, G.; Ferbinteanu, M.; Ramos Fernandez, E. V.; Sepulveda-Escribano, A.; Wu, H.-H.; Cavani, F.; Rothenberg, G.; Shiju, R. N. Understanding the oxidative dehydrogenation of ethyl lactate to ethyl pyruvate over vanadia/titania catalysts. *Catal. Sci. Technol.* **2018**, *8*, 3737-3747.

(34) Zhang, W.; Ensing, B.; Rothenberg, G.; Shiju, R. N. Designing effective solid catalysts for biomass conversion: Aerobic oxidation of ethyl lactate to ethyl pyruvate. *Green Chem.* **2018**, *20*, 1866-1873.

(35) Zhang, W.; Oulego, P.; Slot, T. K.; Rothenberg, G.; Shiju, N. R. Selective Aerobic Oxidation of Lactate to Pyruvate Catalyzed by Vanadium ‐ Nitrogen ‐ Doped Carbon Nanosheets. *ChemCatChem* **2019**, *11*, 3381-3387.

(36) Zhang, W.; Innocenti, G.; Oulego, P.; Gitis, V.; Wu, H.-H.; Ensing, B.; Cavani, F.; Rothenberg, G.; Shiju, N. R. Highly selective oxidation of ethyl lactate to ethyl pyruvate catalysed by mesoporous vanadia–titania. *ACS Catal.* **2018**, *8*, 2365-2374.

(37) Majjane, A.; Chahine, A.; Et-tabirou, M.; Echchahed, B.; Do, T.-O.; Breen, P. M. X-ray photoelectron spectroscopy (XPS) and FTIR studies of vanadium barium phosphate glasses. *Mater. Chem. Phys.* **2014**, *143*, 779-787.

(38) Benabdelouahab, G. F.; Volta, J. C.; Olier, R. New Insights into VOPO4 Phases Through Their Hydration. *J. Catal.* **1994**, *148*, 334-340.

(39) Zhang, Y.; Li, X.; Ko, J. Highly Efficient Gas Phase Oxidation of Renewable Furfural to Maleic Anhydride over Plate VPO Catalyst. *ChemSusChem* **2018**, *11*, 612-618.

(40) Wang, F.; Dubois, J.-L.; Ueda, W. Catalytic dehydration of glycerol over vanadium phosphate oxides in the presence of molecular oxygen. *J. Catal.* **2009**, *268*, 260-267.

(41) Samotus, B.; Schwimmer, S. Phytic Acid as a Phosphorus Reservoir in the Developing Potato Tuber. *Nature* **1962**, *194*, 578.

Table of Contents

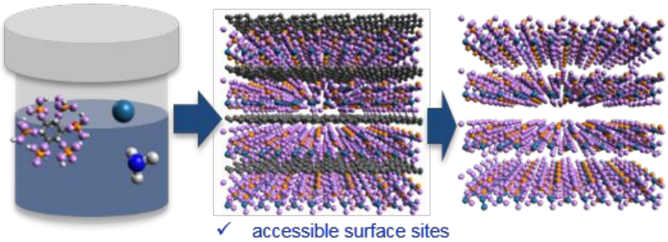

✓ accessible surface sites
✓ V^{4+}/V^{5+} redox sites
✓ Defects and oxygen vacancies

Spot on! A template-free strategy to prepare 2D phosphate nanosheets for selective aerobic oxidation.